Soft Matter

Residual Strain Effects in Needle-Induced Cavitation

Journal:	*Soft Matter*
Manuscript ID	SM-ART-06-2019-001173.R1
Article Type:	Paper
Date Submitted by the Author:	14-Aug-2019
Complete List of Authors:	Barney, Christopher; University of Massachusetts Amherst, Polymer Science And Engineering Zheng, Yue; UCSD, Department of Mechanical and Aerospace Engineering Wu, Shuai; UCSD, Department of Mechanical and Aerospace Engineering Cai, Shengqiang; UCSD, Department of Mechanical and Aerospace Engineering Crosby, Alfred; University of Massachusetts, Polymer Science and Engineering

SCHOLARONE™
Manuscripts

Soft Matter

ARTICLE TYPE

Cite this: DOI: 10.1039/xxxxxxxxxx

Residual Strain Effects in Needle-Induced Cavitation†

Christopher W. Barney,[a] Yue Zheng,[b] Shuai Wu,[b] Shengqiang Cai,[b] and Alfred J. Crosby,*[a]

Received Date
Accepted Date

DOI: 10.1039/xxxxxxxxxx

www.rsc.org/journalname

Needle-induced cavitation (NIC) locally probes the elastic and fracture properties of soft materials, such as gels and biological tissues. Current NIC protocols tend to overestimate properties when compared to traditional techniques. New NIC methods are needed in order to address this issue. NIC measurements consist of two distinct processes, namely 1) the needle insertion process and 2) the cavitation process. The cavitation process is hypothesized to be highly dependent on the initial needle insertion process due to the influence of residual strain below the needle. Retracting the needle before pressurization to a state in which a cylindrical, tube-like fracture is left below the needle tip is experimentally demonstrated to reduce the impact of residual strain on NIC. Verification of the critical cavitation pressure equation in this new geometry is necessary before implementing this retraction NIC protocol. Complementary modeling shows that the change in initial geometry has little effect on the critical cavitation pressure. Together, these measurements demonstrate that needle retraction is a viable experimental protocol for reducing the influence of residual strain, thus enabling the confident measurement of local elastic and fracture properties in soft gels and tissues.

1 Introduction

Cavitation rheology is a developing field coalescing from the independent development of a diverse set of mechanical characterization techniques that capitalize on the underlying physics of cavitation. Among this set are techniques such as needle-induced cavitation (NIC),[1–19] laser-induced cavitation (LIC),[20–23] acoustic-induced cavitation (AIC),[24–27] shockwaved-induced cavitation (SIC),[28–31] and confinement-induced cavitation (CIC).[32–38] A diverse, tunable range of size and time scales between techniques makes cavitation rheology attractive for characterizing soft materials. Needle-induced cavitation (NIC) provides a highly localized probe of the elastic and fracture properties of soft materials, such as gels and biological tissues, that are often difficult to manipulate into traditional mechanical characterization geometries. This technique has the potential to characterize tissues *in vivo* but has been limited by variability in the properties measured as shown in Figure 1.[1–9] The references in Figure 1 measured elastic modulus by at least two techniques and the data indicates that NIC tends to overestimate the modulus compared to traditional mechanical characterization techniques. This trend indicates that new NIC protocols are necessary for characterizing materials properties.

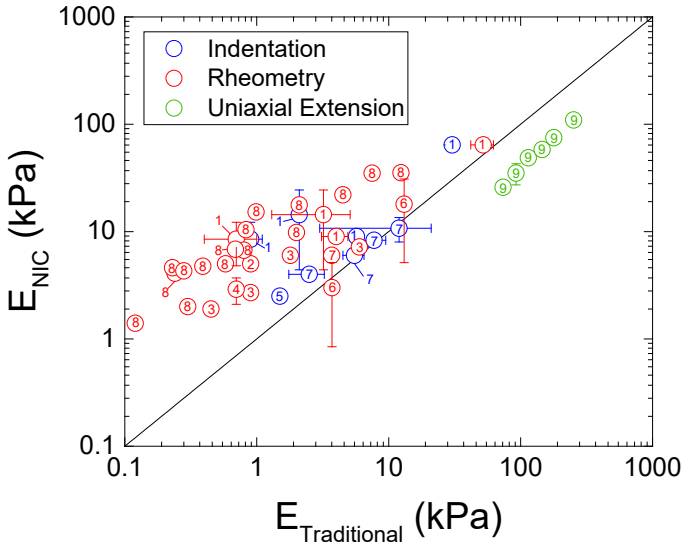

Fig. 1 Plot of elastic modulus measured with needle-induced cavitation against values measured with shear rheometry, indentation, and uniaxial extension from literature.[1–9] The black line is the equivalent point.

Counter to this trend, Raayai-Ardakani et. al recently found that moduli from NIC were significantly lower than those mea-

[a] *Polymer Science and Engineering Department, University of Massachusetts, 120 Governors Drive, Amherst, MA, 01003, USA. Fax: +1 413 545 0082; Tel: +1 423 577 1313; E-mail: crosby@mail.pse.umass.edu*

[b] *Department of Mechanical and Aerospace Engineering, University of California, San Diego, La Jolla, CA 92093, USA.*

† Electronic Supplementary Information (ESI) available: [details of any supplementary information available should be included here]. See DOI: 10.1039/cXsm00000x/

sured from uniaxial extension.[9] They calculated NIC moduli assuming a purely elastic cavitation mechanism, however, based on the interpretation in their more recent work, a fracture mechanism was observed.[39] Fracture necessarily occurs at a pressure below the cavitation threshold which explains the observed discrepancy.[10,40] Bentz et al.[8] recently discussed the trend observed in Figure 1 between measurement techniques and argued that it related to the nature of the crosslinking bond in the gel. However, Bentz et al. did not test if the increase is primarily related to the stress state in the gel resulting from the needle insertion process.

The NIC measurement consists of two distinct processes, namely 1) an initial needle insertion process and 2) a subsequent cavitation process. While the cavitation process has received much attention in the literature, the needle insertion process has largely remained unspecified.[41] This ambiguity in needle insertion protocol leaves NIC measurements vulnerable to scatter and shifts imparted due to the presence of residual strain at the needle tip, which may lead to a misinterpretation of data.

To estimate the impact of residual strain on NIC, assume that the critical pressure at the tip of a needle inserted beyond the point of puncture can be represented as the superposition of the cavitation pressure in a fully relaxed system and the average pressure needed to overcome the residual stress at the tip. The cavitation pressure can be approximated as the elastic modulus E,[42] and the residual stress can be approximated by E multiplied by a measure of the compressive strains at the needle tip,

$$P_c = P_{cav} + P_{Residual\ Strain} \approx E\left(1+\frac{\delta - l}{R_{out}}\right) \tag{1}$$

where P_c is the critical pressure, δ is displacement of the indenter in reference to the undeformed surface, l is the axial length of the fracture after puncture, and R_{out} is the outer radius of the indenter. For flat-tipped needles, often employed in NIC, the compressive strain can become quite large upon insertion and is not fully released upon puncturing.[43–45] As supported below, $\delta - l \approx 10^{-3}$ m typically and $R_{out} \approx 10^{-4}$ m such that the residual strain term can often be an order of magnitude greater than the cavitation term. Strategies to address this limitation in sensitivity and accuracy are needed to extend the impact and usefulness of NIC.

This paper first assesses the residual strain hypothesis mentioned above and then introduces a new needle insertion protocol that creates an initially cylindrical NIC geometry. The theoretical form of the critical cavitation pressure equation in the altered geometry is then verified with finite element modeling. Critical pressures of the new geometry are experimentally demonstrated to conform to the spherical cavitation equation. This difference in behavior is understood through the concept of residual strain at the needle tip. A scaling argument is presented for estimating the retraction distance needed to produce the cylindrical NIC geometry. These findings have large implications for the characterization of soft solids and biological tissues where pre-strain can result from sample geometry or boundary conditions.

2 Experimental

2.1 Methods

2.1.1 Indentation.

Cylindrical, flat probe indentation was used to measure the elastic modulus of samples. Force and displacement were monitored using a TA.XT Plus Texture Analyzer from Texture Technologies with a 50 N load cell. Each sample was tested at a displacement rate of 0.1 mm/s using a 2 mm diameter flat, cylindrical steel probe attached directly to the load cell and a turnaround force of 20 mN. A schematic of the setup with a representative plot of the data is shown in Supplementary Figure S1. Modulus was calculated using Equation (2) which contains a confinement correction term to Hertzian contact developed by Shull et. al where a is contact radius, h is sample height, and C is the experimentally observed sample compliance.[46]

$$E = \frac{3}{8a}\frac{1}{C}\left[1+1.33\frac{a}{h}+1.33\left(\frac{a}{h}\right)^3\right]^{-1} \tag{2}$$

The critical adhesive strain energy release rate G_c^A between steel and the PDMS blends was estimated using Equation (3) where F_{peak} is the peak separation force.[46]

$$G_c^A = \frac{3F_{peak}^2}{32\pi E R_{out}^3} \tag{3}$$

Equation (3) describes how to determine the critical strain energy release rate for separating the interface between a flat, cylindrical probe and the gel. The format of this equation incorporates several assumptions, most importantly that the system is assumed to be fully elastic, thus independent of rate, temperature, or loading history. We use this form here to provide a means of comparing scaling relations developed below, which are based on a quasi-elastic treatment of the materials systems as related to the NIC measurements. A more complete discussion on measurement of contact mechanics methods for quantifying polymer interface adhesion can be found in these references.[46–51]

2.1.2 Puncture.

Puncture tests were performed using a different configuration on the same instrument mentioned in Section 2.1.1. For this test, blunt tipped needles of various size sourced from the Hamilton Company were rigidly mounted. The sample was raised onto the needle at a displacement rate of 0.1 mm/s with force and displacement being monitored through the base of the sample. Visualization of the deformation was obtained using an EO-1312C color CCD camera from Edmund Optics. A schematic of the setup and representative plot of the data is shown in Supplementary Figure S2. The peak puncture force F_c was used in order to calculate Γ_o according to Equation (4), assuming an energy-limited puncture.[45]

$$F_c = \Gamma_o R_{out} \tag{4}$$

Γ_o is a measure of the fracture nucleation energy and may be thought to scale with the critical energy release rate G_c.[41,45]

This journal is © The Royal Society of Chemistry [year]

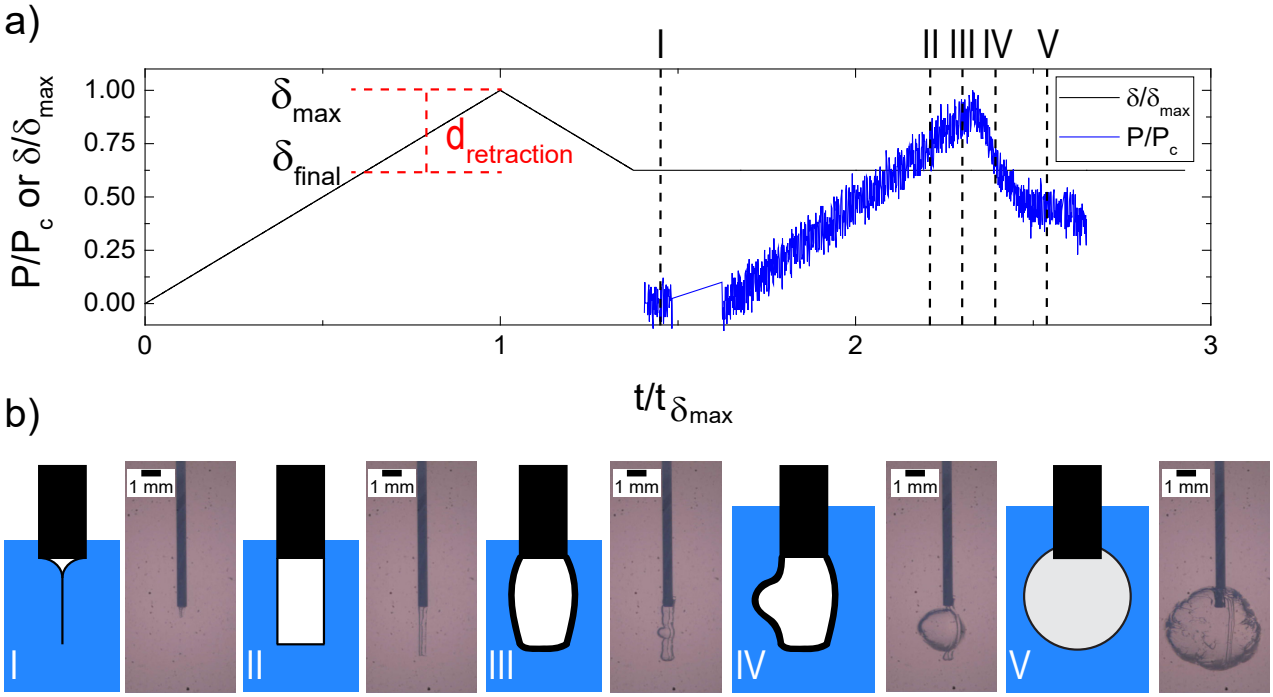

Fig. 2 a) Normalized displacement and pressure vs time for the needle insertion process. Needle insertion happens at a constant speed to a maximum displacement δ_{max} beyond the point of puncture. The needle is then retracted a controlled distance $d_{retraction}$ at the same speed before being held at a final displacement δ_{final}. b) Schematic and images of a needle in a gel at different points of the insertion and cavitation processes.

2.1.3 Needle-Induced Cavitation (NIC).

A needle-induced cavitation setup was designed to monitor force and displacement of the needle, pressure at the tip of the needle, and visualize the needle tip during testing. Visualization of the deformations at the tip and monitoring of the needle force and displacement was achieved using the instrumentation discussed in Section 2.1.2. Blunt tipped steel needles were purchased from the Hamilton Company. Control of the pressure was achieved using a 1 mL glass Hamilton syringe in a Nexus 6000 syringe pump purchased from Chemyx. Pressure was monitored using a PX309-300G5v pressure sensor purchased from Omega Engineering and interfaced with a custom LabView program. Together, the pressure sensor fittings, syringe, and adapter connecting the system had a total volume of ~2.5 mL. During air injection tests, fittings for the pressure sensor were filled with water leaving ~2 mL of compressible volume in the pressure system implying a maximum gauge pressure of ~100 kPa when injecting air. A representative plot of the data along with the visualization gathered on this setup is contained in Figure 2 as well as in Supplementary Figure S3 and Supplementary Video SV1.

The needle insertion protocol defined in this paper is shown in Figure 2a. It is specified as inserting the needle to a maximum displacement δ_{max} beyond the point of puncture. The needle is then retracted a given distance $d_{retraction}$ before being held at a final displacement $\delta_{final} = \delta_{max} - d_{retraction}$. The insertion and retraction speeds are set equal to each other and referred to as $\dot{\delta}$. A schematic of the needle in the gel at different points during the insertion and pressurization process is shown in Figure 2b.

Needle-induced cavitation is performed by inserting a needle connected to a syringe into a sample and pressurizing the fluid with the syringe. Once a critical pressure is realized, rapid expansion of the sample at the tip of the needle is observed. When this deformation is driven by elasticity, it can be represented by Equation (5),

$$P_c = \frac{C_1 \gamma}{R_{in}} + C_2 E \tag{5}$$

where γ is the interfacial tension between the injected fluid and sample, R_{in} is the inner radius of the needle, and C_1 and C_2 are constants.[6] Values for the constants in Equation (5) are typically assumed to be those from the theoretical treatment of an initially spherical void in an infinite, incompressible solid which gives $C_1 = 2$ and $C_2 = \frac{5}{6}$.[6,52]

When expansion at the needle tip is driven by fracture, the critical pressure is modeled with the linear elastic solution for a penny-shaped crack as shown in Equation (6).[5,53]

$$P_f = \sqrt{\frac{\pi E G_c}{3 R_{in}}} \tag{6}$$

2.1.4 Simulations.

Cylindrical void expansion at a blunt needle tip was simulated using the finite element software ABAQUS (Version 6.13). A schematic of the finite element model nodes is shown in Supplementary Figure S4. Aspect ratio of the void L/R is defined as axial length of the void L divided by radius of the void R. The geometry is assumed to be axisymmetric. Height and radius of the sample block are 100 and 50 times R respectively. The needle modulus is five orders of magnitude greater than the surrounding sample, making it effectively rigid. The sample block is assumed to be

PDMS Blend Name	Cure Time (hr)	Prepolymer:Curing Agent Weight Ratio	Weight Fraction in Linear Chains	E (kPa)
20.5	24	20:1	0.5	80.7±3.5
20.6	24	20:1	0.6	125.3±3.2
30.7	18	30:1	0.7	48.4±4.5
30.7	24	30:1	0.7	62.2±2.2
40.5	24	40:1	0.5	4.5±0.5
40.95	24	40:1	0.95	48.8±3.0

Table 1 Definition of the prepolymer:curing agent ratio and weight fraction of Sylgard®184 diluted with non-reactive linear PDMS chains for different silicone blends

nearly incompressible with a Poisson's ratio $\nu = 0.49999975$. The model is meshed with 8-node biquadratic axisymmetric quadrilateral hybrid elements with reduced integration (CAX8RH), and the mesh is greatly refined around the cavity as shown in Supplementary Figure S4. Four aspect ratios (L/R = 1, 3, 5, and 7 with total respective number of elements 76,046, 82,280, 96,892, and 107,064) are used to quantify changes in critical pressure. The top and bottom sides of the sample cylinder were fixed along the axial direction, but each can slide freely in the radial direction. Pressure was applied to the inner wall of the cylindrical void. Experimental NIC measurements were performed at size scales above those where interfacial tension was relevant and is thus not accounted for in simulations. Simulations were used to test the alteration of C_2 from the spherical value typically assumed in Equation (5).

2.2 Materials

Acrylic triblock gels are a common system for NIC studies due to their highly elastic nature and thermoreversible behavior.[3,7,10,54–56] ABA copolymers of a poly(n-butyl acrylate) midblock with poly(methyl methacrylate) end blocks were kindly provided by Kuraray Co., Ltd and used as received. Gel permeation chromatography and nuclear magnetic resonance spectroscopy were used to determine that the weight average molecular weight of each end block is 25 kg/mol and the mid block is 104 kg/mol with Đ=1.06. Notation for these gels is defined as $A_{25}B_{104}A_{25}$. 2-ethyl-1-hexanol was purchased from Sigma Aldrich and used as received. Samples were prepared by mixing 15 mL of 2-ethyl-1-hexanol with $A_{25}B_{104}A_{25}$ to a polymer volume fraction of 0.07 ($E = 5.2 \pm 0.2$ kPa from indentation) in a 20 mL scintillation vial. The vial was firmly capped and then heated to 110°C for 6 hours after which the warm solution was stirred in a vortex mixer before heating under the same conditions for another 6 hours. Samples were translucent and appeared homogeneous in composition after the final heating step. Samples were cooled by immediate removal from the oven and left at room temperature (22°C) for several hours until fully cooled.

Silicone blends were chosen as a material system due to their flexibility in tuning elastic and fracture properties by simultaneously altering the crosslink density and swelling ratio in the system.[41] 350 cSt trimethylsiloxy terminated linear polydimethylsiloxane (PDMS) chains were purchased from Gelest, Inc. and used as received. A Sylgard®184 kit was purchased from Krayden, Inc. and used as received. Silicone blends were produced by mixing the prepolymer and curing agent at a given ratio and then diluting that mixture to a certain weight fraction with non-reactive linear chains. The notation defined for these blends is "g prepolymer/1 g curing agent.diluted weight fraction of reactive network". For example, a 30.7 PDMS sample would be made

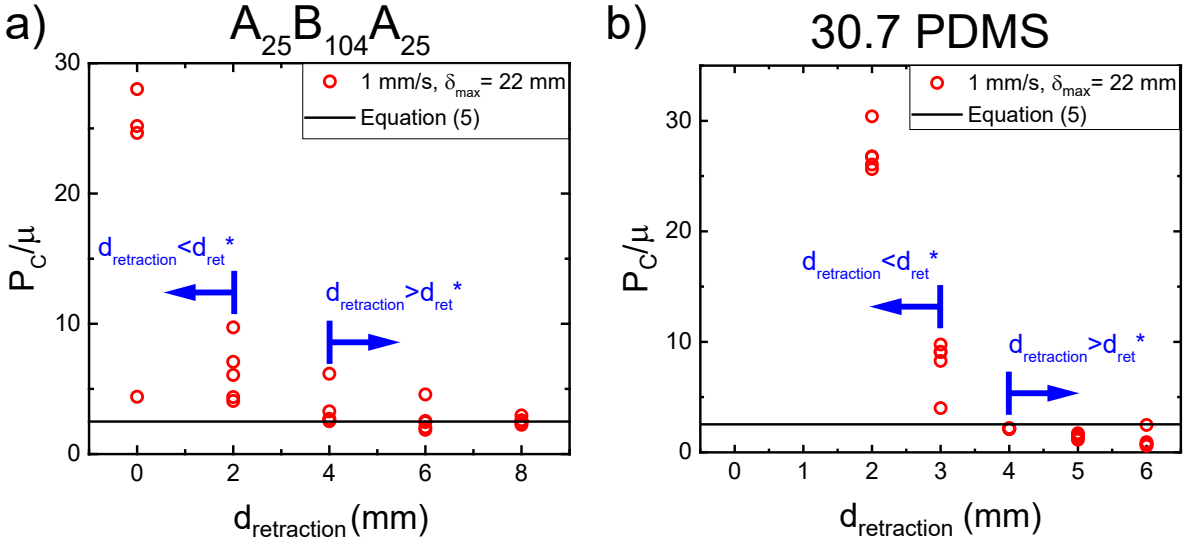

Fig. 3 Plots of critical pressure P_c normalized by the shear modulus μ against $d_{retract}$ for the a) $A_{25}B_{104}A_{25}$ gel and b) 30.7 PDMS blend where (R_{in}, R_{out})=(130,232) μm, $\dot{\delta}$=1 mm/s, δ_{max}=22 mm, and $\dot{V}$=500 μL/min in the $A_{25}B_{104}A_{25}$ gel and $\dot{V}$=50 μL/min in the 30.7 PDMS blend. At small $d_{retraction}$ large pressures with high variability for each gel is observed. At bigger values of $d_{retraction}$ the data becomes more consistent and the critical pressures approach Equation (5).

This journal is © The Royal Society of Chemistry [year]

using a 30:1 prepolymer:curing agent ratio that was then mixed with nonreactive linear chains to a weight fraction of 0.7. Table 1 contains a list of all the blends and their assigned names along with elastic modulus quantified from indentation. The silicone blends were all mixed before curing and degassed for 15 minutes. After degassing each 30.7 sample used for the NIC survey experiment was heated to 70°C and cured for 18 hours. After degassing each sample meant for the critical retraction distance experiment was heated to 70°C and cured for 24 hours. Samples were cooled by immediate removal from the oven and left at room temperature (22°C) for several hours until fully cooled.

3 Needle-Induced Cavitation (NIC) With Retraction

The needle insertion protocol shown in Figure 2 introduces $\dot{\delta}$, δ_{max}, and $d_{retraction}$ as experimental variables that may influence the NIC measurement. An experimental survey probing their impact on the NIC measurement was performed. In addition, the gel chemistry, needle size (R_{in}, R_{out}), and fluid reservoir compression rate $\dot{V}$ were all systematically altered. Full details of the experimental conditions are contained in the Supplementary Information. Plots of P_c/μ against $d_{retraction}$ for the $A_{25}B_{104}A_{25}$ gel at different $\dot{\delta}$, δ_{max}, $\dot{V}$, and (R_{in}, R_{out}) are contained in Supplementary Figure S5. No consistent trend strong enough to be distinguished from $d_{retraction}$ was observed in the data. These results suggest that $d_{retraction}$ is the most important experimental parameter in NIC.

The independence of critical pressure on needle size is unexpected. Equations (5) and (6) predict that P_c should scale with R_{in}^{-1} or $R_{in}^{-1/2}$ when cavitation or fracture is observed, respectively.[1,4,5,7,11,13] This observation is due to an insensitivity to the interfacial tension in the needle sizes used in this study. For the $A_{25}B_{104}A_{25}$ gel, the capillary pressure is predicted to be ~0.7 kPa for the smallest needle used in this study while the experimental variability in pressure is $\sim \pm 1$ kPa.

Plots of P_c normalized by shear modulus μ against $d_{retraction}$ for different gel chemistries are shown in Figure 3. Plots showing all the gel chemistry data gathered with variations in $\dot{\delta}$ and δ_{max} are shown in Supplementary Figure S6, though the trends are similar to those observed in Figure 3. A trend is observed where small retraction distances lead to high pressures and variability, while large retraction distances are associated with more consistent data and pressure values closer to those predicted by Equation (5). This trend of reduced critical pressure is associated with a transition across a critical retraction distance d_{ret}^* where the gel peels from the needle tip leaving a cylindrical tube-like fracture below, as shown in Figure 2b for the $A_{25}B_{104}A_{25}$ gel. Supplementary videos SV1 and SV2, and SV3 and SV4 show the NIC deformation with the needle tip in both the contacting and non-contacting state for the $A_{25}B_{104}A_{25}$ gel and 30.7 PDMS blend, respectively. While experiments at a retraction distance of zero were not conducted for the 30.7 PDMS, the data for the five retraction distances measured are consistent with the trend observed in the $A_{25}B_{104}A_{25}$ gel. The appearance of a cylindrical, tube-like fracture below the needle indicates that the gel is no longer applying large compressive forces to the opening of the needle reducing the residual strain contribution to the pressure for unstable expansion. These findings indicate that critical pressure values will converge to Equation (5) once $d_{retraction} > d_{ret}^*$.

The cylindrical void geometry observed in experiments is markedly different from the spherical void assumed by Equation (5). Simulated expansion of a cylindrical void of varying aspect ratios at the tip of a needle is shown in Figure 4. The change in initial geometry does not significantly alter the critical pressure point. Previous simulations of NIC have similarly concluded that the divergence from the spherical geometry has little effect on the critical pressure behavior.[9,57] This finding implies that Equation

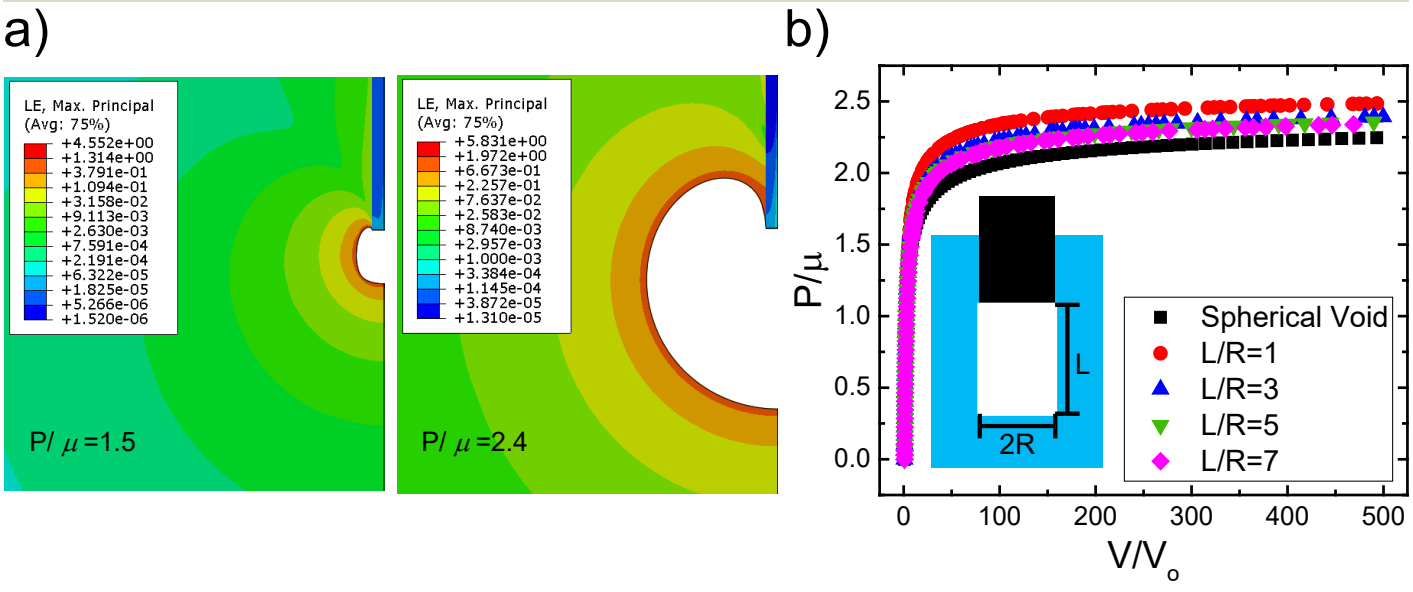

Fig. 4 a) Contour map of the principal stress for a cylinder with $L/R = 3$. b) Plot of P/μ against the volumetric stretch ratio of cavities of varying aspect ratio. This modeling shows that the critical pressure value is relatively insensitive to the altered geometry.

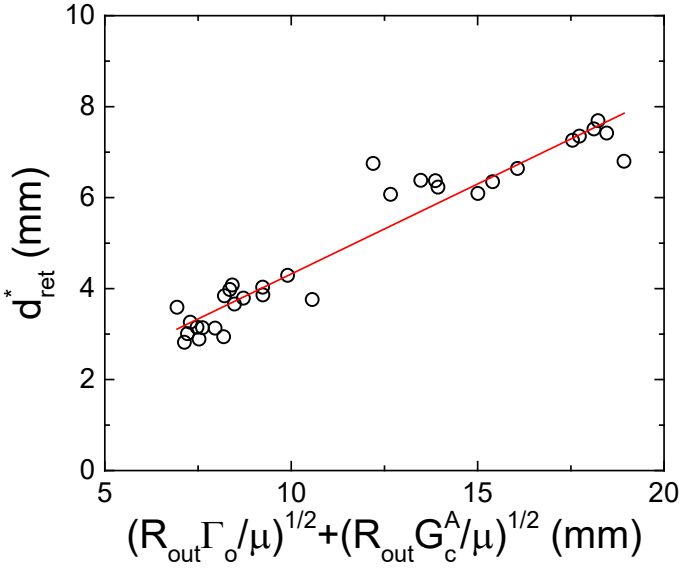

Fig. 5 Plot of experimentally measured d^*_{ret} against the scaling found in Equation (10).The black circles represent data measured on the silicone blends and the red line represents a linear fit of the data. Note that the data follows a linear relationship when plotted in this manner.

(5) adequately describes the critical pressure for cylindrical NIC. However, Figure 3 shows that Equation (5) overestimates the critical pressure for the 30.7 PDMS blend. The 30.7 PDMS blend is a stiff gel ($E = 48.4 \pm 4.5$ kPa) and expansion of the cavity occurs in a steady, non-axisymmetric manner and the pressure time profile, as seen in Supplementary Video SV4, has a smooth peak indicating that 30.7 PDMS blend exhibits fracture behavior.

4 Critical Retraction Distance

4.1 Scaling Critical Retraction Distance

The transition upon needle retraction between a contacting and non-contacting state, shown schematically in Supplementary Figure S7, at the needle tip creates a cylindrical geometry that is insensitive to residual strain. This condition occurs when $d_{retraction} \geq d^*_{ret}$. The critical retraction distance d^*_{ret}, is related to the puncture and fracture propagation process of needle insertion and the adhesive peel process at the interface between the needle and gel upon retraction. Accordingly, d^*_{ret} scales with the elasticity of the gel, cohesive fracture energy of the gel, the interfacial fracture energy between the needle and gel, and indenter geometry. The distance required to relax compressive strains, d_{comp}, and the distance required to separate the needle from the gel, d_{peel}, are considered distinct contributions to d^*_{ret}, such that:

$$d^*_{ret} = d_{comp} + d_{peel} \tag{7}$$

The scaling of d_{peel} is determined by substituting $F_{peel} = 8\mu R_{out} d_{peel}$ into Equation (3). The scaling of d_{comp} can be determined by calculating G_c in the puncture geometry. The derivation presented here is simple and a more complete treatment of the subject has been presented first by Stevenson and Ab-Malek and later by Shergold and Fleck.[58,59] The fracture nucleation energy Γ_o scales with G_c which can be defined as the change in stored potential energy U_e per area A of new surface created.

$$\Gamma_o \sim G_c = -\frac{dU_e}{dA} \tag{8}$$

The elastic energy released can be approximated as $dU_e = -\mu\varepsilon^2 dV$ with ε and V being a measure of the compressive strains and volume of strained material below the indenter respectively. The volume of strained material is given by $dV = \pi R^2_{out} dl$ where l is the axial length of the fracture. The area of new surface created as the crack advances is given as $dA = 2\pi R_{out} dl$. Substituion into Equation (8) gives

$$\Gamma_o \sim \mu\varepsilon^2 R_{out} \tag{9}$$

Treating the compressive strains below the indenter as a Hertzian block gives $\varepsilon = \frac{d_{comp}}{R_{out}}$ which gives the scaling of d_{comp}.[41] Substituting the scalings for d_{comp} and d_{peel} into Equation (7) gives Equation (10).

$$d^*_{ret} = d_{comp} + d_{peel} \sim \sqrt{\frac{R_{out}\Gamma_o}{\mu}} + \sqrt{\frac{R_{out}G_c^A}{\mu}} \tag{10}$$

Figure 5 shows the collapse of d^*_{ret} when plotted against Equation (10). Rearranging Equation (10) the relative contribution of d_{peel} to d^*_{ret} is determined by the ratio G_c^A/Γ_o.

$$d^*_{ret} \sim \sqrt{\frac{R_{out}\Gamma_o}{\mu}}\left(1 + \sqrt{\frac{G_c^A}{\Gamma_o}}\right) \tag{11}$$

Values of Γ_o are typically between 10 and 1000 J/m^2 while typical values for the van der Waals dominated adhesion between two surfaces in intimate contact are around 0.1 J/m^2.[45,47,60] This implies that in most systems the ratio $G_c^A/\Gamma_o \approx 10^{-(2\text{-}4)}$, thus making d^*_{ret} dominated by d_{comp}.

4.2 Estimating Critical Retraction Distance

Equation (11) demonstrates that d^*_{ret} is a function of both the geometry and material properties, thus providing a physical understanding of what properties and parameters control the development of residual stress related to NIC. Although informative and potentially useful in the implementation of NIC, Equation (11) cannot be used *a priori* to design a specific protocol for systems where the materials properties are unknown. For using NIC in these cases, we provide two recommendations based on the findings presented in this manuscript. First, for systems where direct visualization of the needle tip during insertion is possible, users can visually determine d^*_{ret} by observing the cylindrical tube below the needle tip. Second, for systems where visualization is nontrivial, users can estimate d^*_{ret} by using the force and displacement data of the needle to observe a change in stiffness.

Force and displacement on the needle during insertion and retraction is shown in Figure 6a. Five distinct stages appear on this plot.[41] First is the loading stage (i) which refers to the initial elastic loading regime before puncture occurs.[45] Second is the embedding stage (ii) which occurs after puncture where further insertion is resisted by a sliding friction on the needle walls and a local failure stress supported at the needle tip. Third is the shearing/decompression stage (iii) which occurs in the early stage of

This journal is © The Royal Society of Chemistry [year]

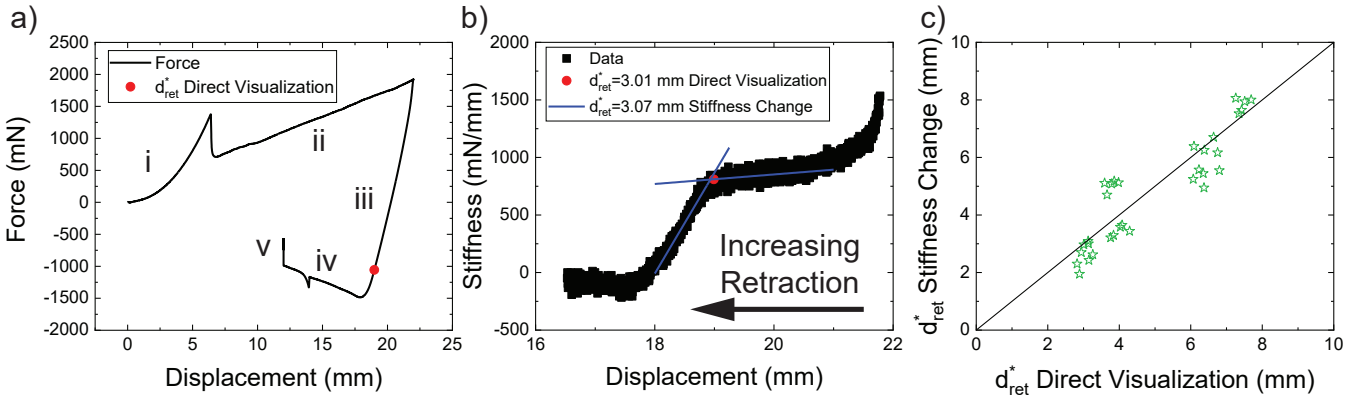

Fig. 6 a) Force against displacement of the needle during insertion and retraction for a representative run on the 20.5 PDMS Blend. d^*_{ret} measured from direct visualization of the needle tip is marked with a red circle. b) Stiffness against displacement during needle retraction across the transition between stages iii and iv. The intersection of two linear fits of the stiffness before and after the blend peels from the needle tip is shown to closely agree with the estimate of d^*_{ret} from direct visualization. c) Plot of d^*_{ret} measured with the stiffness change method (no visualization) and d^*_{ret} measured by direct visualization on the PDMS blends.

needle retraction where the force response is determined by static friction on the needle walls and compression below the needle tip. Fourth is the pullout stage (iv) where the force response is determined by a sliding friction at the needle walls. Fifth is the holding stage (v) where the needle is held at a constant displacement where a relaxation in the friction at the needle walls results in a decay in the force.[41]

d^*_{ret} denotes the onset of the transition between the static contact in stage (iii) and the sliding contact in stage (iv) and is marked by a red circle in Figure6a. The transition between stages (iii) and (iv) is not obvious when force is plotted against displacement; however, this transition becomes clear when the stiffness ($dF/d\delta$) is plotted against displacement as in Figure 6b. The intersection of linear fits of stiffness against displacement before and after the onset of the transition from stage (iii) to (iv) can be used to estimate d^*_{ret}. Figure 6c displays estimates of d^*_{ret} measured by the stiffness change method (no visualization) against estimates from direct visualization of the needle tip and good agreement is observed between the two values. These results show that monitoring the force and displacement data on the needle can be used to estimate d^*_{ret} in samples where visualization is not possible.

5 Conclusions

NIC measurements are a strong function of the needle insertion protocol. Retracting the needle after insertion leaves a cylindrical, tube-like fracture below the needle tip at a critical retraction distance. This critical retraction distance scales with the fracture properties of the gel, elasticity of the gel, and geometry of the indenter and was insensitive to the adhesive interaction between the needle and gel. The cylindrical NIC geometry displays better agreement with theoretical models for the onset of cavitation of a spherical void in soft gels due to a reduction in residual strain below the needle tip. Complementary modeling suggests that altering the initial defect geometry to a cylinder does not significantly alter the critical pressure value. These results demonstrate that needle retraction is a viable method for reducing the influence of residual strain on NIC measurements. This is particularly important to soft gels and biological tissues where strain can arise from complex shapes and boundary conditions.

6 Acknowledgements

The authors acknowledge the support of the Office of Naval Research (ONR grant number N00014-17-1-2056). The authors also thank Kuraray Co., Ltd for providing the acrylic triblock copolymers used in this study.

References

1 L. E. Jansen, N. P. Birch, J. D. Schiffman, A. J. Crosby and S. R. Peyton, *Journal of the mechanical behavior of biomedical materials*, 2015, **50**, 299–307.
2 P. Fei, S. J. Wood, Y. Chen and K. A. Cavicchi, *Langmuir*, 2015, **31**, 492–498.
3 S. M. Hashemnejad and S. Kundu, *Soft Matter*, 2015, **11**, 4315–4325.
4 J. A. Zimberlin and A. J. Crosby, *Journal of Polymer Science Part B: Polymer physics*, 2010, **45**, 1423–1427.
5 S. Kundu and A. J. Crosby, *Soft Matter*, 2009, **5**, 3963.
6 J. A. Zimberlin, N. Sanabria-DeLong, G. N. Tew and A. J. Crosby, *Soft Matter*, 2007, **3**, 763.
7 A. Delbos, J. Cui, S. Fakhouri and A. J. Crosby, *Soft Matter*, 2012, **8**, 8204.
8 K. C. Bentz, N. Sultan and D. A. Savin, *Soft Matter*, 2018.
9 S. Raayai Ardakani, Z. Chen, D. Earl and T. Cohen, *Soft Matter*, 2018.
10 S. B. Hutchens, S. Fakhouri and A. J. Crosby, *Soft Matter*, 2016, **12**, 2557–2566.
11 B. R. Frieberg, R.-s. Garatsa, R. L. Jones, E. P. Chan, J. O. B. Iii, B. Crawshaw and X. M. Liu, *Soft Matter*, 2017, 1–5.
12 K. C. Bentz, S. E. Walley and D. A. Savin, *Soft Matter*, 2016, **12**, 4991–5001.
13 J. Cui, C. H. Lee, A. Delbos, J. J. McManus and A. J. Crosby, *Soft Matter*, 2011, **7**, 7827.

14 S. M. Hashemnejad, M. M. Huda, N. Rai and S. Kundu, *ACS Omega*, 2017, **2**, 1864–1874.

15 J. A. Zimberlin, J. J. McManus and A. J. Crosby, *Soft Matter*, 2010, **6**, 3632.

16 N. Teo and S. C. Jana, *Langmuir*, 2018, **34**, 8581–8590.

17 Y. Liu, A. Lloyd, G. Guzman and K. A. Cavicchi, *Macromolecules*, 2011, **44**, 8622–8630.

18 A. Blumlein, N. Williams and J. J. McManus, *Scientific Reports*, 2017, **7**, 1–10.

19 S. Polio, A. Kundu, C. Dougan, N. Birch, D. E. Aurien-Blajeni, J. Schiffman, A. Crosby and S. Peyton, *Plos One*, 2018, **13**, 1–17.

20 I. Akhatov, O. Lindau, A. Topolnikov, R. Mettin, N. Vakhitova and W. Lauterborn, *Physics of Fluids*, 2001, **13**, 2805–2819.

21 I. Akhatov, N. Vakhitova, A. Topolnikov, K. Zakirov, B. Wolfrum, T. Kurz, O. Lindau, R. Mettin and W. Lauterborn, *Experimental Thermal and Fluid Science*, 2001, **26**, 731–737.

22 L. Martí-López, R. Ocaña, E. Piñeiro and A. Asensio, *Physics Procedia*, 2011, **12**, 442–451.

23 J. B. Estrada, C. Barajas, D. L. Henann, E. Johnsen and C. Franck, *Journal of the Mechanics and Physics of Solids*, 2018, **112**, 291–317.

24 A. D. Maxwell, T.-Y. Wang, C. A. Cain, J. B. Fowlkes, O. A. Sapozhnikov, M. R. Bailey and Z. Xu, *The Journal of the Acoustical Society of America*, 2011, **130**, 1888–1898.

25 Z. Xu, T. L. Hall, J. B. Fowlkes and C. A. Cain, *The Journal of the Acoustical Society of America*, 2007, **122**, 229–236.

26 V. A. Khokhlova, M. R. Bailey, J. A. Reed, B. W. Cunitz, P. J. Kaczkowski and L. A. Crum, *The Journal of the Acoustical Society of America*, 2006, **119**, 1834–1848.

27 P. Movahed, W. Kreider, A. D. Maxwell, S. B. Hutchens and J. B. Freund, *The Journal of the Acoustical Society of America*, 2016, **140**, 1374–1386.

28 M. C. Bustamante, D. Singh and D. S. Cronin, *Experimental Mechanics*, 2017, 1–20.

29 Y. Hong, M. Sarntinoranont, G. Subhash, S. Canchi and M. A. King, *Experimental Mechanics*, 2016, **56**, 97–109.

30 W. Kang, A. Ashfaq, T. O'Shaughnessy and A. Bagchi, *Acta Biomaterialia*, 2017, **67**, 295–306.

31 S. Canchi, K. Kelly, Y. Hong, M. A. King, G. Subhash and M. Sarntinoranont, *Journal of the Mechanical Behavior of Biomedical Materials*, 2017, **74**, 261–273.

32 A. N. Gent and P. Lindley, *Proceedings of the Royal Society of London Series A Mathematical and Physical*, 1959, **249**, 195–205.

33 A. N. Gent and B. Park, *Journal of Materials Science*, 1984, **19**, 1947–1956.

34 K. Cho, A. N. Gent and P. S. Lam, *Journal of Materials Science*, 1987, **22**, 2899–2905.

35 K. Cho and A. N. Gent, *Journal of Materials Science*, 1988, **23**, 141–144.

36 H. Lakrout, P. Sergot and C. Creton, *Journal of Adhesion*, 1999, **69**, 307–359.

37 A. J. Crosby, K. R. Shull, H. Lakrout and C. Creton, *Journal of Applied Physics*, 2000, **88**, 2956–2966.

38 S. Lin, Y. Mao, R. Radovitzky and X. Zhao, *Journal of the Mechanics and Physics of Solids*, 2017, **106**, 229–256.

39 S. Raayai-Ardakani, D. R. Earl and T. Cohen, *Soft Matter*, 2019.

40 Y. Y. Lin and C. Y. Hui, *International Journal of Fracture*, 2004, **126**, 205–221.

41 S. Fakhouri, *Doctoral Dissertations*, 2015.

42 A. N. Gent and D. A. Tompkins, *Journal of Applied Physics*, 1969, **40**, 2520–2525.

43 D. I. Livingston, G. S. Yeh, P. Rohall and S. D. Gehman, *Journal of Applied Polymer Science*, 1961, **V**, 442–451.

44 W.-c. Lin, K. J. Otim, J. L. Lenhart, P. J. Cole and K. R. Shull, *Journal of Materials Research*, 2009, **24**, 957–965.

45 S. Fakhouri, S. B. Hutchens and A. J. Crosby, *Soft matter*, 2015, **11**, 4723–4730.

46 K. R. Shull, D. Ahn, W.-L. Chen, C. M. Flanigan and A. J. Crosby, *Macromolecular Chemistry and Physics*, 1998, **199**, 489–511.

47 K. R. Shull, *Materials Science and Engineering: R: Reports*, 2002, **36**, 1–45.

48 D. Maugis and M. Barquins, *Journal of Physics D: Applied Physics*, 1978, **11**, 1989–2023.

49 M. Barquins and D. Maugis, *Journal of Adhesion*, 1981, **13**, 53–65.

50 C. Creton and M. Ciccotti, *Reports on Progress in Physics*, 2016, **79**, 046601.

51 K. Johnson, K. Kendall and A. D. Roberts, *Proceedings of the Royal Society of London. Series A, Mathematical and Physical Sciences*, 1971, **324**, 301–313.

52 A. N. Gent and D. A. Tompkins, *Rubber Chemistry and Technology*, 1970, **43**, 873–877.

53 A. N. Gent and C. Wang, *Journal of Materials Science*, 1991, **26**, 3392–3395.

54 P. L. Drzal and K. R. Shull, *Macromolecules*, 2003, **36**, 2000–2008.

55 M. E. Seitz, W. R. Burghardt, K. T. Faber and K. R. Shull, *Macromolecules*, 2007, **40**, 1218–1226.

56 M. E. Seitz, D. Martina, T. Baumberger, V. R. Krishnan, C.-Y. Hui and K. R. Shull, *Soft Matter*, 2009, **5**, 447–456.

57 S. B. Hutchens and A. J. Crosby, *Soft matter*, 2014, **10**, 3679–3684.

58 A. Stevenson and K. Ab Malek, *Rubber Chemistry and Technology*, 1994, **67**, 743–760.

59 O. a. Shergold and N. a. Fleck, *Proceedings of the Royal Society A: Mathematical, Physical and Engineering Sciences*, 2004, **460**, 3037–3058.

60 S. Rattan, L. Li, H. K. Lau, A. J. Crosby and K. L. Kiick, *Soft Matter*, 2018, **14**, 3478–3489.

This journal is © The Royal Society of Chemistry [year]

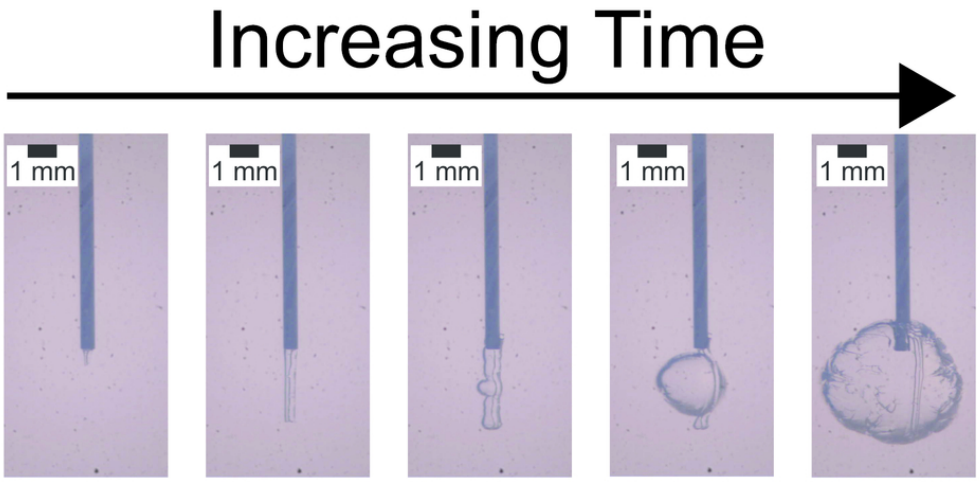

80x40mm (300 x 300 DPI)